Core-controlled polymorphism in virus-like particles

Jingchuan Sun*†, Chris DuFort‡, Marie-Christine Daniel‡, Ayaluru Murali§, Chao Chen‡, Kodetham Gopinath§, Barry Stein¶, Mrinmoy De‖, Vincent M. Rotello‖, Andreas Holzenburg*§†, C. Cheng Kao§, and Bogdan Dragnea‡**

Departments of §Biochemistry and Biophysics and *Biology, and †Microscopy and Imaging Center, Texas A&M University, College Station, TX 77843; ‡Department of Chemistry and ¶Indiana Molecular Biology Institute, Indiana University, Bloomington, IN 47405; and ‖Department of Chemistry, University of Massachusetts, Amherst, MA 01002

Communicated by Charles S. Parmenter, Indiana University, Bloomington, IN, November 29, 2006 (received for review August 8, 2006)

This study concerns the self-assembly of virus-like particles (VLPs) composed of an icosahedral virus protein coat encapsulating a functionalized spherical nanoparticle core. The recent development of efficient methods for VLP self-assembly has opened the way to structural studies. Using electron microscopy with image reconstruction, the structures of several VLPs obtained from brome mosaic virus capsid proteins and gold nanoparticles were elucidated. Varying the gold core diameter provides control over the capsid structure. The number of subunits required for a complete capsid increases with the core diameter. The packaging efficiency is a function of the number of capsid protein subunits per gold nanoparticle. VLPs of varying diameters were found to resemble to three classes of viral particles found in cells ($T = 1$, 2, and 3). As a consequence of their regularity, VLPs form three-dimensional crystals under the same conditions as the wild-type virus. The crystals represent a form of metallodielectric material that exhibits optical properties influenced by multipolar plasmonic coupling.

metamaterials | protein cage | self-assembly | surface plasmon | virus assembly

Engineered virus capsids and protein cage structures have shown increasing promise as therapeutic and diagnostic vectors (1–6), imaging agents (7–10), and as templates and microreactors for advanced nanomaterials synthesis (11–17). Here, we address the rules for the formation of symmetric protein cages consisting of viral capsid subunits formed over a functionalized inorganic nanoparticle core, called virus-like particles (VLPs).

VLPs provide an example of how biomimetic self-organization can combine the natural characteristics of virus capsids with the exquisite physical properties of nanoparticles (18–20). Interactions between the artificial cargo and the protein carrier affects both the self-assembly and the stability of the resulting structure, yet very little is known about them. Progress toward the basic development and the practical use of VLPs requires an understanding of how relevant parameters contribute to complex formation.

Symmetric VLPs may provide a technology for therapeutic or diagnostic agent delivery that is improved over amorphous shell nanoparticles that are already known to be efficient in similar applications (21). The advantage of a regular surface protein motif is that the binding domains are functionally identical by virtue of their equivalent environment. It has been shown in several situations that receptor-mediated targeting can be achieved even when using amorphous coatings (22). However, the principle challenges for nanoparticle delivery currently include: limited life-time in body fluids, nanoparticle transduction across the cellular membrane, avoidance of the exocytotic pathways, and target specificity. To optimize their infectivity, viruses have evolved to overcome these challenges. We still must learn how to apply virus strategies to targeted delivery. A simple question is central to this objective. What is the minimum set of requirements that a cargo must satisfy to promote encapsidation without interfering with its carrier? Answering this question for a model system should provide novel benchmarks for future development of nanoparticle delivery platforms. The present paper is a step in this direction.

Major factors that could affect the efficiency of VLP formation include the chemical and physical properties of the core surface. We have determined that a gold core functionalized with a coating of carboxylated polyethylene glycol (PEG) can allow efficient assembly of VLPs (18). Here, we report some first steps in a systematic examination of how these cores influence the capsid structures and functional properties. The ultimate goal is to determine the minimal set of properties that an artificial core has to possess to promote the assembly of a symmetric viral protein structure around it. The main question to be addressed is then: what is the relation between the core surface properties and the capsid morphology? In this paper, we are specifically focusing on the gold core size.

We used brome mosaic virus (BMV) as a model system to provide the protein cage for our VLPs because it can yield an abundance of capsid. BMV is a small icosahedral virus (≈280 Å) that infects *Poaceae* species (23). The crystal structure of the native BMV has been solved and is composed of 180 identical proteins of 20 kDa that form pentameric or hexameric subunits in a $T = 3$ lattice (24). The basic subunit of assembly is a dimer. The BMV capsid is compact at low to moderate ionic strength buffers with pH below 5.0, but experiences a profound structural transition when the pH is increased from 5 to 7 (25). Mg^{2+} stabilizes the capsid at pH levels close to neutrality, where reversible expansion occurs without dissociation. At pH above 7.5 and ionic strength higher than 0.5 M, the capsid dissociates and the viral RNA precipitates. Upon reestablishment of low pH and ionic strength, reassociation occurs. Wild-type BMV is composed of three nearly identical classes of particles that contain separate RNA1, RNA2, or RNA3, and RNA4. In plants and in a replication-competent host for BMV replication, *Saccharomyces cerevisiae*, empty particles of the $T = 3$ geometry and a smaller pseudo$T = 2$ capsid have been observed (26–28). A $T = 1$ geometry forms *in vitro* after cleavage of the N-terminal 63 or 35 amino acid residues of the capsid protein (CP) by trypsin or endogenous proteinase (29). The interaction between RNA and protein is proposed to mediate the transition between the pseudo$T = 2$ and the $T = 3$ forms of BMV, and the length of the RNA could mediate a switch from $T = 1$ to pseudo$T = 2$ capsid (28). The relatively nonspecific association between the negatively charged nucleic acid core and the dense positive charge of the internal capsid surface make BMV an ideal system for nanoparticle encapsidation. The ability to produce structurally distinct viral particles suggests that BMV capsids can be used to produce structurally and functionally distinct constructs in a regulated manner.

Results and Discussion

Supporting Information. For further details, see supporting information (SI) Figs. 6–11.

Author contributions: C.C.K. and B.D. designed research; J.S., C.D., M.-C.D., and C.C. performed research; K.G., B.S., M.D., and V.M.R. contributed new reagents/analytic tools; J.S., C.D., A.M., and A.H. analyzed data; and B.D. wrote the paper.

The authors declare no conflict of interest.

Abbreviations: VLP, virus-like particle; PEG, polyethylene glycol; BMV, brome mosaic virus; CP, capsid protein; AFM, atomic force microscopy.

**To whom correspondence should be addressed. E-mail: dragnea@indiana.edu.

This article contains supporting information online at www.pnas.org/cgi/content/full/0610542104/DC1.

© 2007 by The National Academy of Sciences of the USA

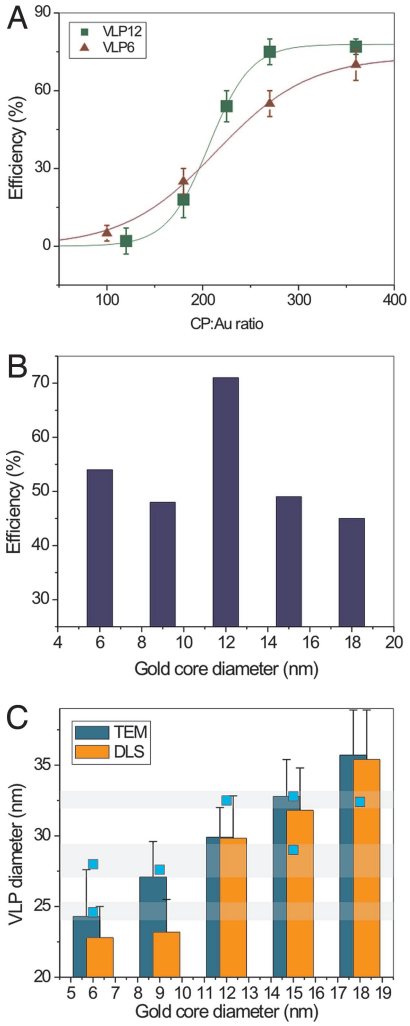

Fig. 1. Incorporation efficiency. (*A*) Relative incorporation efficiency as a function of CP/Au. A threshold greater than ≈100 protein subunits per gold nanoparticle is required for assembly. Lines are sigmoidal fits to data. (*B*) Maximum incorporation efficiency was reached for 12-nm cores. All data in *A* and *B* are from TEM. (*C*) VLP average diameter increases uniformly with the core diameter (CP/Au = 270:1) by DLS and TEM. However, size histograms show that different populations of particles coexist. The square dots represent the most frequent VLP diameters (local histogram maxima).

Incorporation Efficiency. When gold particles are absent from the assembly mixture, a larger number of empty capsids are observed in TEM micrographs than in the presence of Au (18). Incorporation of gold nanoparticles is therefore the result of the competition between the formation of empty capsids and other aggregates and VLPs. In the absence of a kinetic model to quantitatively describe this competition, we define efficiency of the VLP synthesis as the ratio between the final number of complete VLP particles formed and the total number of Au particles.

For all gold core sizes, the relative efficiency of encapsidation depends on the initial CP to gold nanoparticle ratio (CP/Au) with a threshold value above ≈100 protein subunits per gold nanoparticle (Fig. 1*A*). At low CP/Au ratios, the efficiency of VLP_6 is greater than VLP_{12}. At the ratio of 270:1 used throughout this paper, efficiency peaks at ≈70% for VLP_{12}, in agreement with earlier findings, suggesting that the Au cores act as nucleating centers for capsid self-assembly (Fig. 1*B*). For VLP_{12}, there are typically <5% empty capsids and very few naked gold particles (<1% of the total amount of gold). VLP_6 and VLP_9 also yielded preparations homogeneous in size and shape (SI Fig. 6). However, the assembling efficiencies were noticeably lower, mainly due to an increase in the number of empty particles seen in electron micrographs. For VLP_{15} and VLP_{18}, the gold particles became heterogeneous in size and shape (SI Fig. 6). Fewer than 45% of the gold particles had a complete capsid. Correspondingly, we observed an increase in the proportion of empty particles, naked gold particles, gold cores that were incompletely coated with protein, and VLPs with irregular protein coats.

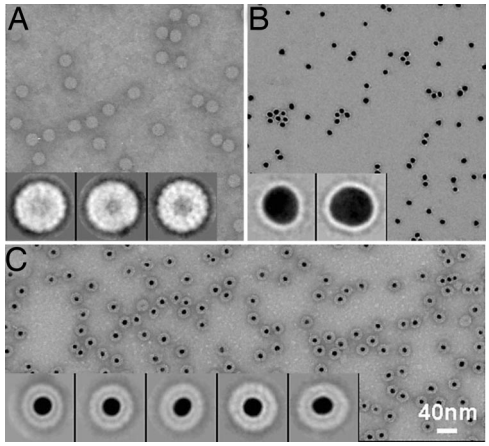

Fig. 2. Typical spreads of R3BMV (*A*), PEG-Au (*B*), and VLP_{12} (*C*) as used for single-particle image reconstruction. PEG-Au lacks any finer structural detail, and the density modulations with native BMV and the 12 nm VLPs suggest distinct protein subunit architecture.

Mean VLP diameters correlated well with gold core diameters (Fig. 1*C*). However, analysis of VLP size histograms indicates that there are at least three subpopulations of particles: 25, 29, and 32 nm (dots in Fig. 1*C* and SI Fig. 8). The VLPs measured for 3D image reconstruction also yielded the three basic diameters, although somewhat smaller: 21–22, 26, and 28 nm. The source of the difference in these measurements is not clear. It may come from sample preparations or digitization procedures. Au cores of 15 nm and larger were more heterogeneous, in terms of size and shape, than the smaller cores. However, when the VLPs obtained from 15-nm cores were sorted by diameter, similar distributions of VLP (21, 26, and 28 nm) were observed. These results suggest that the formation of VLPs is constrained by subunit interactions.

Native BMV capsids have been reported to exist in three conformations that vary in the number of subunits: $T = 1$ (60 subunits), pseudo$T = 2$ (120 subunits), and $T = 3$ (180 subunits) (28, 30). These conformations have been proposed to reflect RNA features that can thus direct the assembly between alternate structural pathways (28). The presence of distinguishable sizes of Au-containing VLPs and the efficiency of encapsidation lead us to hypothesize that the diameter of the core is mimicking the properties of the RNA to induce distinct VLP structures. To determine whether there is support for this hypothesis, we determined the VLP structures.

Two-Dimensional Crystal Analysis of R3BMV and VLP. The high degree of homogeneity of the VLP samples with cores of 6, 9, and 12 nm encouraged us to attempt to grow 2D crystals for TEM analysis. Two-dimensional crystals of all three preparations and R3BMV (control) were obtained with the lipid monolayer method using negatively charged lipid (Fig. 2*A*). Fourier transforms reveal reflections that go readily out to the eighth order, suggesting a resolution of ≈3 nm. Each virus capsid in the averaged 2D projection map of the crystal (space group *p3*) has six similar sized densities around a central mass. The arrangement of the densities is consistent with the pattern of pentamers and hexamers on the

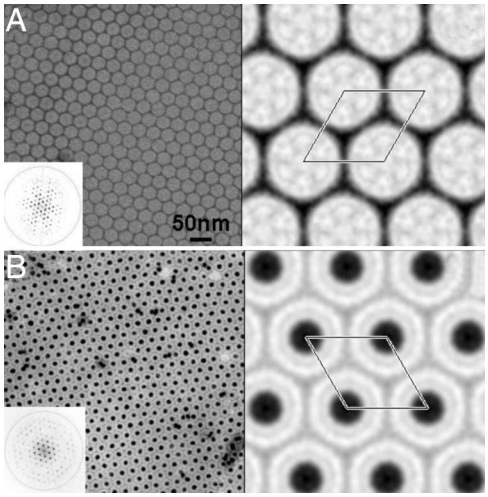

Fig. 3. Negative-stain electron micrographs, Fourier transforms (inserts), and corresponding Fourier projection maps. (*A*) R3BMV 2D crystal. The lattice constant is 26 nm (one unit cell is drawn), and the arrangement of the densities suggests a $T = 3$ structure. (*B*) VLP_{12} 2D lattice. The lattice constant is 25 nm.

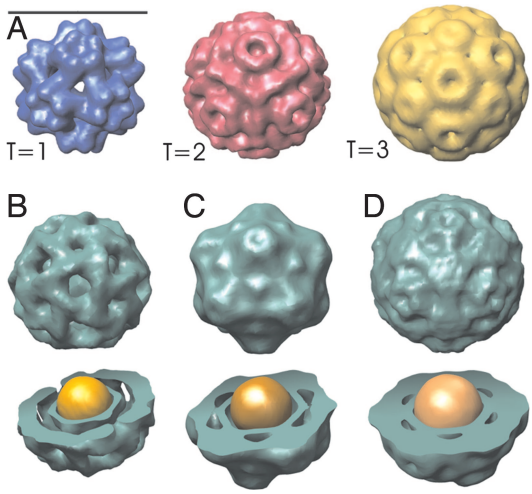

Fig. 4. Three-dimensional reconstructions of R3BMV and VLP using negative stain data. (*A*) $T = 1$, 2, and 3 models of BMV capsids. The $T = 1$ and pseudo$T = 2$ structures were obtained from the VIPER database (54) and ref. 24. The $T = 3$ structure is the reconstructed image of R3BMV in this work. (Scale bar, 210 Å.) (*B*) VLP_6 is characterized by the absence of electron density at the threefold symmetry axes. Its structure and diameter bring it close to a $T = 1$ capsid. (*C*) The VLP_9 structure is reminiscent of a pseudo$T = 2$. The presence of electron density at the threefold axes distinguishes it from the VLP_6 structure. (*D*) The VLP_{12} shape resembles more to the spherical shape of R3BMV although it still lacks clear evidence of hexameric capsomers. Concentric layering is a characteristic of all VLPs.

capsid of $T = 3$ BMV. However, the unit cell parameters of different crystals of R3BMV varied from 25 to 27 nm, which may be the result of variations in the size of individual capsids or in the packing density. Note that the average diameter of R3BMV from single-particle analysis is 28 nm, which is larger than the dimension measured in the 2D crystals. This might be due to the capsids being more densely packed in the crystal when compared with the situation in solution. The changes in 2D lattice dimensions may also reflect different crystal forms that serendipitously have similar lattice constants.

The unit cell dimension of VLP_{12} crystals is ≈25 nm, smaller than the R3BMV and the average diameter of VLP_{12} in solution. Due to readily discernable gaps in the density going from the center toward the periphery, three separate zones, i.e., the Au core, the PEG shell, and the protein capsid, can be identified (Fig. 2*B*). The density in the gap between the PEG and the protein is not entirely homogeneous and appears to delineate putative contact points between specific capsid sites and the PEG shell. Hexagonally packed VLP_6 crystals have a unit cell size of 22 ± 1 nm.

Single-Particle Reconstructions. To elucidate additional structural features of VLP_{12},VLP_9, and VLP_6, we performed single-particle analysis with 3D reconstruction. The samples were spread on a carbon grid, along with R3BMV (Fig. 3). We noticed that the single-particle spread of the VLP_{12} contained more empty particles in comparison to the particles in the 2D crystal, suggesting that the core-containing VLPs are preferentially incorporated into the 2D lattice.

Classification and averaging of >2,000 R3BMV particles show that individual capsids (Fig. 3*A Inset*) have the same arrangement of hexamers and pentamers as the crystal projection (Fig. 2*A*), although the crystal projection had higher resolution. The PEG shell of the PEG-Au can be observed in the original electron micrograph (Fig. 3*B*) and is much clearer in the class averages (Fig. 3*B Inset*).

The 3D reconstruction of R3BMV (Fig. 4*A*) resulted in a model that corresponds well to the published CryoEM structure of $T = 3$ BMV, with 12 pentamers and 20 hexamers per capsid (total of 180 subunits) (28), demonstrating the validity of this approach. To compare the similarity between our 3D reconstruction and the structure from the CryoEM database, we calculated the Fourier shell correlation between the two structures (SI Fig. 7, thick line). The two models are correlated up to 3 nm (with 0.5-nm threshold), which is satisfactory if one considers the differences in sample preparation and imaging conditions.

The 3D projection of VLP_{12} contains 12 pentamers (Fig. 4*D*). There is clear evidence of density at the hexamer position, with a quasi-sixfold symmetry. However, it is not as prominent as the fivefolds, which may be due to structural variation related to the cores and to negative stain and drying. The small diameter (25 nm) seems to suggest that VLP_{12} may have a 120-unit capsid; however, it is possible that the viral capsids shrunk slightly during sample processing for TEM imaging (31). Therefore, it is likely that VLP_{12} is a $T = 3$ particle in solution.

The VLP_6 and VLP_9 3D reconstructions clearly lack hexamers and therefore are associated with a different structure than $T = 3$. Thus, VLP_9 is similar to a pseudo$T = 2$ arrangement previously determined for the RNA-controlled 120-unit BMV capsid (24) (Fig. 4*C*). VLP_6 has a characteristic latticework of holes penetrating the surface, which renders it similar to the previously reported $T = 1$ structure obtained by treatment of the wild-type $T = 3$ virus with $CaCl_2$ and crystallized from sodium malonate (29) (Fig. 4*B*).

Interestingly, a section through the PEG layer in all three of the VLPs appears to have a hexagonal shape around the gold core. In the VLP_{12}, the spaces are less obvious, suggesting a tighter packaging within these particles. Because the PEG is attached uniformly around the gold, the altered distribution may be imposed by the capsid subunits, possibly the flexible N terminus, which intercalates into the RNA (25). The hexagonal shape results in notable spaces where no apparent contact was observed between the PEG and the capsid. These results demonstrate that the conformation of the VLPs can be manipulated simply by changing the diameter of the core. Furthermore, the conformations observed are good molecular mimics of structures of BMV and BMV assembly intermediates found in cells.

Given that there are clear structural differences between VLP_6 and VLP_{12}, a different ratio of the capsid to core is expected to be required for efficient formation of the two VLPs. Indeed, Fig. 1*A* indicates that, at low CP/Au ratios, VLP_6 forms with greater efficiency than VLP_{12}.

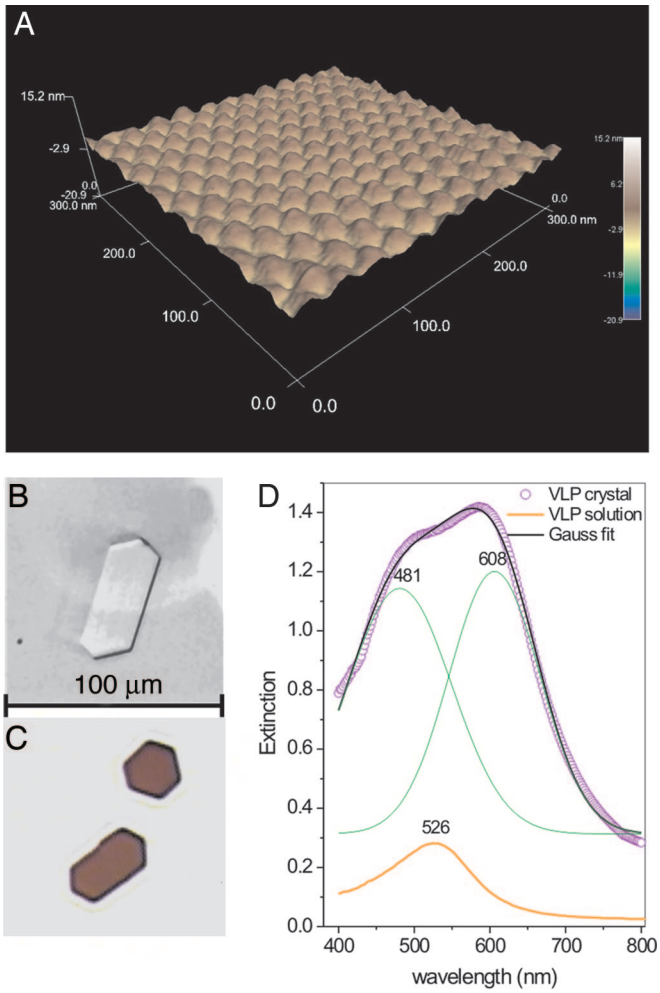

Fig. 5. VLP crystal properties. (*A*) AC-mode AFM image of the face of a R3BMV crystal immersed in its mother liquor. Transmission optical images of R3BMV (*B*) and VLP_{12} crystals (*C*). (*D*) Optical spectrum of a 3D VLP crystal is distinct from the single resonance characteristic of dilute VLP_{12} solutions.

VLP Size Determined by Atomic Force Microscopy (AFM) and Spectroscopy. Because there is some discrepancy between the diameters expected of the BMV capsid and that of the VLPs determined by TEM, we used AFM liquid-imaging of 3D crystals to determine the lattice constant and thus the capsid diameter at physiological conditions. Because of the relatively large radius of curvature of the AFM probe, no capsid structures were observed in Fig. 5*A*, and the probe cannot get in between individual viruses to accurately determine their shapes. However, the individual capsids are clearly distinct, and lateral lattice period measurements should not be affected.

Using a Fourier transform of the AFM pattern of defect-free areas on the crystal surface, we consistently measured a lattice constant of 27.8 ± 0.5 nm for R3BMV, in good agreement with the dimensions expected for BMV (25) (Fig. 5*A*). Because the TEM-measured 2D lattice constant was 26 nm, we conclude that there was ≈7% linear compression due to vacuum conditions used in TEM. The same effect is expected to compress the VLP_{12} 2D crystal. However, due to the Au nanoparticle inside, the compression factor may be different and remains unknown.

Spectroscopic Properties of 3D Crystals of Mixtures of R3BMV and VLP_{12}. An adjustment of the diameters of the VLPs measured by AFM suggests that the VLP_{12} may be sufficiently similar to BMV capsids to form cocrystals. In support of this idea, both R3BMV and VLP crystallize in the rhombohedral group (Fig. 5 *B* and *C*). Therefore, cocrystallization of VLP_{12} with R3BMV was attempted. Cocrystals were obtained for every concentration ratio tested (see SI Fig. 9). The mixed crystals are red colored with a color intensity proportional to the relative concentration of VLP_{12}, which excludes the possibility of segregation during crystallization. These results provide a strong indication that BMV and VLP_{12} capsids are sufficiently similar in solution to grow crystals. Because the concentration of VLPs in the initial crystallization drop is lower than that of R3BMV, pure VLP crystals are usually significantly smaller than R3BMV crystals. Their small size (typically <10–20 μm, laterally) makes them difficult to handle. Therefore, we used absorption spectroscopy to obtain more information on these 3D crystals.

Because one would expect a significant deviation of the optical spectrum for small gold interparticle distances due to multipolar effects on coupling (33), we analyzed the transmitted light through VLP_{12} crystals (Fig. 5*D*). The absorption spectrum shows a double hump that can be obtained by superposition of two Gaussian lineshapes, one centered at 481 nm and the other centered at 608 nm. In contrast, a dilute VLP_{12} solution exhibited a single peak due to the well known surface plasmon resonance at 526 nm (Fig. 5*D*).

Capsid Assembly Control. Insight into empty capsid formation has been obtained in recent years from theoretical (33–37) and *in vitro* experimental studies (31, 38, 39). In this case, a sequential assembly principle has been proposed in which either preformed intermediates or individual structural subunits adhere to a proto-capsomer or initial nucleation center to form a capsid (33, 40). However, when the nucleic acid core is present, capsid nucleation experiments follow different kinetics (41). The sequential model does not provide an explicit role of the nucleic acid in the assembly process nor does it show how identical protein subunits form a pentamer or a hexamer.

A recent alternative model posits that a disordered nucleoprotein aggregate resembling a reverse micelle assembles initially and is followed by subsequent condensation and conformational change of the protein on the micelle surface to yield the capsid quaternary structure (42, 43). In this context, capsid assembly around artificial cores opens new possibilities for experimental virus assembly modeling because the thermodynamic properties of the core can be controlled.

The isotropic experimental core model should provide an accessible departure point to test the most general aspects of virus self-assembly modeling that include contributions of the nucleic acid core. We propose that the VLP system described here, with its structurally uniform core, is an experimental example of the model. By varying a single parameter, namely the core radius, we obtained a strong correlation with assembly efficiency. In the following, we analyze several of the features of this VLP assembly from the perspective of the two models.

The protein concentration at which the assembly experiments have been carried (30 μM) is well above the critical concentration for empty capsid assembly (≈10 μM) (44). Therefore, the existence of a threshold CP/Au ratio for VLP formation, even when the protein concentration is larger than the critical concentration for empty capsids, signifies that there is a rapid initial association step between protein subunits and the negatively charged cores that is independent of the structural requirements for capsid formation. In support of this view, an increased number of empty capsids was observed in the absence of Au cores. Although protein association with Au-PEG cores also occurs for nanoparticles larger than 12 nm, the resulting VLPs do not form crystals and therefore are likely to possess a disorganized protein shell, with low incorporation efficiency. It thus appears that icosahedral symmetry is somehow critical to the process of assembly or to particle stability.

If the number of CP subunits per core is insufficient to form a

complete shell, larger aggregates will form by coalescence of the incomplete nanoparticle/protein aggregates (19). In turn, this results in low encapsidation efficiencies and the presence of a threshold CP/Au ratio.

Smaller cores result in smaller capsids (Fig. 4). However, in the absence of a perturbation from the core, empty capsid growth results almost exclusively in a $T = 3$ structure. $T = 1$ capsids similar to VLP_6 are observed when the N termini of the CP are cleaved between amino acids 35 and 36 (30). The cores are thus screening the N termini interactions normally occurring in empty capsids made of intact protein. With the N termini interaction screened, the VLP capsid assembles from the minimum number of subunits needed to enclose the core inside a closed shell. In the view of the micelle model, smaller cores would recruit less protein subunits at the initial step so that a smaller T number is more likely to occur. Interestingly, in the *in vitro* assembly of BMV, $T = 3$ particles will assemble from intact proteins in the presence of the natural BMV genome, but pseudo$T = 2$ particles can be obtained using engineered RNA (28). We note that pentamers are clearly present in all reconstructed VLPs (Fig. 4), whereas evidence for hexamers is unclear in the reconstructed images of VLP_{12}. This feature suggests that pentamers may be required precursors for VLP formation. The requirement would be in agreement with earlier findings from kinetic analysis of empty capsid assembly (45), whereas VLP_{12} may represent a "frozen" intermediate with incompletely organized protein subunits at the threefold symmetry positions. Another explanation, however, could be that the hexamers are less stable than the pentamers, and they are the first to give way upon the lattice distortion due to drying in acidic conditions.

Finally, it is instructive to analyze the relation between the size of the artificial core and the packaging efficiency in comparison to the packaging of the three BMV genomic RNAs. BMV RNA3 is ≈2,100 nt in length, ≈67% of the length of BMV RNA1, a difference comparable to that between VLP_9 (packaging efficiency of 48%) and VLP_{12} (efficiency of 74%). These results predict that RNA3 would be packaged inefficiently unless it is copackaged along with an RNA that can make up the difference in mass relative to RNA1. Indeed, examination of the RNAs in R3BMV revealed a 1:1 stoichiometry with RNA4. At this point, VLP assembly seems to reflect a duality between the micelle and sequential mechanisms. We believe that future experiments of this type, with focus on parameters such as the surface charge density at constant core radius, should test the dual mechanism suggested here.

VLP_{12} Crystals as Metallodielectric Metamaterials. Metamaterials have optical (or more general, electromagnetic) properties determined by their organized structure rather than inherited directly from the individual subunits (45). Optical properties of metallodielectric metamaterials composed of resonant metal inclusions in a dielectric matrix with subwavelength lattice periods have been predicted theoretically (46, 47). Such 3D structures have lattice constants between 10 and 100 nm and are difficult to synthesize with current technologies. The question of whether 3D VLP crystals may offer a solution to this problem is discussed below.

The optical transmission spectrum of a VLP crystal is different from that of a dilute solution of VLPs (Fig. 5). One possible explanation is that, due to the optically flat parallel surfaces of the crystal, multiple beam interference could occur, with the effect of modulating transmission across the spectral range of the white light source (400–900 nm). To test this hypothesis, we have calculated the transmission of a thin film of adjustable thickness using an effective medium dielectric constant approach (48). Assuming a lattice constant of 28 nm for VLP_{12}, which corresponds to a metal filling factor $f = 0.06$, the only adjustable parameter to fit the observed maximum extinction is the film thickness. By this method, the film thickness found from the experimental maximum extinction is 160 nm for the VLP crystals in Fig. 5. The thin film approach in combination with the effective medium approximation does not reproduce, however, the double spectral feature in Fig. 5 so that its origins are not related to multiple beam interference.

We propose that the observed double peak is the signature of multipolar coupling between the gold cores that leads to plasmonic band formation. This feature cannot be accounted for by the Maxwell–Garnett theory (48) used in calculating the effective medium dielectric constant because it does not include contributions beyond those from dipolar. However, plasmon hybridization occurs when coupling between adjacent gold particles becomes significant and introduction of multipolar terms becomes required (49). The expected result is two absorption bands, one shifted to the blue and the other to the red of the surface plasmon peak of the single particle, similar to our observations from VLP_{12} crystals (Fig. 5). Such plasmonic band splittings in metallo-dielectric materials have been predicted theoretically, but never demonstrated experimentally in 3D structures (46, 49).

By this argument, the VLP crystal qualifies as an optical metamaterial having properties determined by both structure and material composition. Note that, for concentrated VLP solutions, the splitting is not observed because of a much broader spectral response. Therefore, crystals obtained from VLPs represent a convenient way to fabricate highly regular 3D structures with lattice constants in the sub-100-nm range. As suggested here, the lattice period can be varied by using different core sizes and possibly, in the future, by using engineered CPs and anisotropic cores.

Materials and Methods

VLP Assembly on Au-PEG with Different Diameters. Functionalized gold cores (Au-PEG) with different diameters (6, 9, 12, 15, 18, and 20 nm) were synthesized as reported (19). The Au-PEG nanoparticle solutions are routinely screened by dynamic light scattering (Malvern, Mastersizer 2000) and UV-Vis spectroscopy for correct average size and polydispersity before encapsidation and transmission electron microscopy characterization. To form VLPs, Au-PEG particles are added to BMV CP at molar ratio of 1:270. VLP assembly has been carried out at neutral pH following the same protocol used in Chen *et al.* (18), but with a protein concentration of 30 μM. The efficiency of encapsulation was measured as the ratio of VLPs having an Au core completely encapsulated by a capsid to the total number of gold nanoparticles (irrespective of level of encapsulation) present in a given area of the electron micrograph. Throughout the paper, VLP_x will designate a virus-like particle prepared with a gold core of "x"-nm diameter ($x = 6$, 9, 12, 15, or 18 nm). Native BMV containing RNA3 and RNA4 that serve as controls for the structural analysis of VLPs are extracted from tobacco plants. Briefly, plants were infiltrated with *Agrobacterium* to express the BMV 1a and 2a replication proteins (no RNA1 or RNA2 are produced in this case), and also RNA3. The RNA3 will replicate and result in the transcription of RNA4, which can be translated to produce the CP. Because there are no BMV RNA1 and RNA2 in the cells, the only RNAs packaged are RNA3 and RNA4. This preparation is called R3BMV.

Transmission Electron Microscopy. A JEOL 1010 TEM operated at 100 kV was used for routine negative staining and direct size measurements. Two-dimensional crystals were grown according to the lipid monolayer method as described by Sun *et al.* (50). Briefly, 15 μl of the R3BMV or VLP solution at 0.6 mg/ml concentration in buffer A [50 mM Mes, pH 6.0/1 mM $MgCl_2$/40 mM Na_2SO_4/50 mM $(NH_4)_2SO_4$] were added to a custom-designed Teflon well of 4 mm in width and 1 mm in depth. A total of 0.3 μl of mixed lipid solution of 30 μg/ml DOPS and 90 μg/ml egg phosphotidylcholine (Avanti Lipids, Alabaster, AL, catalog nos. 850375 and 840051) in chloroform/hexane (1:1, vol/vol) was layered on top of the protein solution and incubated overnight at 4°C in a humidity chamber. The 2D crystals were transferred to a carbon-coated copper grid, washed with distilled water, and negatively stained with an aqueous solution of 1% uranyl acetate. Two-dimensional crystals imaging

has been done at a calibrated magnification of ×38,900 using a JEOL (Tokyo, Japan) 1200EX transmission electron microscope operated at an acceleration voltage of 100 kV. Electron micrographs were digitalized using an Epson (Long Beach, CA) Projection 3200 scanner at 1,200 dpi, corresponding to 5.1 Å/pixel at the specimen level. Crystallographic image processing was carried out with the CRISP software package (51).

Three-Dimensional Reconstruction of R3BMV and VLP. A total of 2.6 μl of R3BMV or VLP at 50 μg/ml in 100 mM Mes (pH 6.0) was adsorbed to a glow-discharged carbon-coated copper grid, negatively stained, imaged, and digitized as described above. The EMAN software package was used for single-particle image analysis and 3D reconstruction (52). For all preparations, >1,000 particles were selected from the digitized electron micrographs using EMAN's *boxer* routine. The images were then filtered to remove high- and low-frequency noise, translationally and rotationally aligned, classified, and averaged without applying symmetry.

For 3D reconstruction, an initial model was produced from the centered particles with EMAN's *starticos* program and subjected to eight cycles of refinement by projection matching. The final 3D reconstruction was visualized with the University of California, Santa Cruz, Chimera software (53). The 3D CryoEM structure of BMV was downloaded as CCP4 format from VIPER EMDB (54) (VIPER ID: em_2bmv and em_3bmv), changed to MRC format with Imagic's *em2em* program, scaled to 5.1 Å/pixel with EMAN's *proc3d*, and aligned to our 3D reconstruction using the *align3D* routine in EMAN (52).

Three-Dimensional Crystallization and AFM. Crystals were grown according to a protocol modified from the one outlined by Lucas *et al.* for BMV (24). Three-dimensional crystals of BMV and VLP have been prepared by the hanging drop vapor diffusion method. BMV and VLP solutions have been concentrated to 2 mg/ml, and crystallization conditions have been explored using a PEG-6000/Ion screen (Hampton Research, Riverside, CA). VLP and BMV crystallize in the same conditions. PEG-6000 (15%) in 0.1 M Tris(hydroxymethyl) methylamine and 3 μl of BMV or VLP solution were mixed together to a drop of ≈6 μl. The drop was hung from a siliconized circular coverslip above a 500-μl solution reservoir. The cover slips were sealed with vacuum grease, and the matrix was stored at 4°C. The first microcrystals appeared overnight. For AFM, crystals of at least 0.3 mm in size have been adsorbed on freshly cleaved mica surfaces. AC mode imaging (MFP3D, Asylum Research, Santa Barbara, CA) on crystals immersed in their mother liquor was done using a soft BioLever probe (0.01 N/m). No other special methods of fixation have been used.

Microcrystal Spectroscopy. Transmission spectra from single crystals immersed in the mother liquor were acquired using an inverted Nikon (Tokyo, Japan) TE300 microscope fitted with a 60-W tungsten white light source, an Acton 300i monochromator, and an EG & G (Salem, MA) SPCM50 photon counting avalanche photodiode module. Optical images were acquired with a CCD camera (Pixera, Los Gatos, CA). Three Nikon FCI microscope objectives were used for the microspectroscopy work: ×10 objective, N.A. 0.25; ×40 objective, N.A. 0.75; and oil ×60 objective, N.A. 1.4.

Conclusion

Nanoparticles can be functionalized to act as nucleating centers efficiently promoting self-assembly of symmetric capsids. The VLP ensembles thus obtained are homogeneous and can be crystallized for high-resolution structural studies. Such crystals may represent a new venue for plasmonic metamaterials. With a single parameter, the gold core diameter, it is possible to switch between several polymorphs that have been already observed for RNA-controlled BMV packaging. The incorporation efficiency is also a function of the gold core diameter, and it reaches a maximum for a gold core of 12 nm. The ability to regulate the formation of specific structures should be important in designing nanoparticles with desired functions. Due to its versatility and possibility of control of the interaction between the anionic core and the protein shell, the nanoparticle VLP concept provides for a future platform for templated self-assembly studies of protein cages.

We thank Dr. W. Schaich and Dr. V. Draguea for useful discussions on plasmonic coupling and crystal growth. This work was supported in part by National Science Foundation (NSF) Grants BES-0322767 and BES 0627875 and MetaCyt (to B.D.), and NSF Grant DMI-0531171 (Nanoscale Science and Engineering Center) (to V.M.R.).

1. Garcea RL, Gissmann L (2004) *Curr Opin Biotechnol* 15:513–517.
2. Cheng WF, Hung CF, Hsu KF, Chai CY, He LM, Polo JM, Slater LA, Ling M, Wu TC (2002) *Hum Gene Ther* 13:553–568.
3. Dietz GPH, Bahr M (2004) *Mol Cell Neurosci* 27:85–131.
4. Ferrari M (2005) *Curr Opin Chem Biol* 9:343–346.
5. Gupta B, Levchenko TS, Torchilin VP (2005) *Adv Drug Delivery Rev* 57:637–651.
6. Khor IW, Lin TW, Langedijk JPM, Johnson JE, Manchester M (2002) *J Virol* 76:4412–4419.
7. Soto CM, Blum AS, Vora GJ, Lebedev N, Meador CE, Won AP, Chatterji A, Johnson JE, Ratna BR (2006) *J Am Chem Soc* 128:5184–5189.
8. Sapsford KE, Soto CM, Blum AS, Chatterji A, Lin TW, Johnson JE, Ligler FS, Ratna BR (2006) *Biosens Bioelectron* 21:1668–1673.
9. Dragnea B, Chen C, Kwak ES, Stein B, Kao CC (2003) *J Am Chem Soc* 125:6374–6375.
10. Boldogkoi Z, Sik A, Denes A, Reichart A, Toldi J, Gerendai I, Kovacs KJ, Palkovits M (2004) *Progr Neurobiol* 72:417–445.
11. Douglas T, Young M (1998) *Nature* 393:152–155.
12. Flynn CE, Lee SW, Peelle BR, Belcher AM (2003) *Acta Mater* 51:5867–5880.
13. Chatterji A, Ochoa WF, Ueno T, Lin TW, Johnson JE (2005) *Nano Lett* 5:597–602.
14. Douglas T, Strable E, Willits D, Aitouchen A, Libera M, Young M (2002) *Adv Mater* 14:415–418.
15. Falkner JC, Turner ME, Bosworth JK, Trentler TJ, Johnson JE, Lin TW, Colvin VL (2005) *J Am Chem Soc* 127:5274–5275.
16. Kramer RM, Li C, Carter DC, Stone MO, Naik RR (2004) *J Am Chem Soc* 126:13282–13286.
17. Vriezema DM, Aragones MC, Elemans J, Cornelissen J, Rowan AE, Nolte RJM (2005) *Chem Rev* 105:1445–1489.
18. Chen C, Daniel M-C, Quinkert Z, De M, Stein B, Chipman PR, Rotello VM, Kao CC, Dragnea B (2006) *Nano Lett* 6:611–616.
19. Loo L, Guenther RH, Basnayake VR, Lommel SA, Franzen S (2006) *J Am Chem Soc* 128:4502–4503.
20. Douglas T, Young M (2006) *Science* 312:873–875.
21. Farokhzad OC, Jon SY, Khadelmhosseini A, Tran TNT, LaVan DA, Langer R (2004) *Cancer Res* 64:7668–7672.
22. Tkachenko AG, Xie H, Coleman D, Glomm W, Ryan J, Anderson MF, Franzen S, Feldheim DL (2003) *J Am Chem Soc* 125:4700–4701.
23. Lane LC (1977) *CMI/AAB Descript Plant Vir* 180:1–4.
24. Lucas RW, Larson SB, McPherson A (2002) *J Mol Biol* 317:95–108.
25. Lane LC (1981) in *Handbook of Plant Virus Infections and Comparative Diagnosis*, ed Kurstak E (Elsevier, Amsterdam), pp 334–376.
26. Choi YG, Rao ALN (2000) *Virology* 275:249–257.
27. Choi YG, Dreher TW, Rao ALN (2002) *Proc Natl Acad Sci USA* 99:655–660.
28. Krol MA, Olson NH, Tate J, Johnson JE, Baker TS, Ahlquist P (1999) *Proc Natl Acad Sci USA* 96:13650–13655.
29. Larson SB, Lucas RW, McPherson A (2005) *J Mol Biol* 346:815–831.
30. Lucas RW, Kuznetsov YG, Larson SB, McPherson A (2001) *Virology* 286:290–303.
31. Cuillel M, Zulauf M, Jacrot B (1983) *J Mol Biol* 164:589–603.
32. Gersten JI, Nitzan A (1985) *Surf Sci* 158:165–189.
33. Zlotnick A (1994) *J Mol Biol* 241:59–67.
34. Zlotnick A (2005) *J Mol Recognit* 18:479–490.
35. Bruinsma RF, Gelbart WM, Reguera D, Rudnick J, Zandi R (2003) *Phys Rev Lett* 90:248101.
36. Hagan MF, Chandler D (2006) *Biophys J* 91:42–54.
37. Rapaport DC (2004) *Phys Rev E* 70:051905.
38. Willits D, Zhao X, Olson N, Baker TS, Zlotnick A, Johnson JE, Douglas T, Young MJ (2003) *Virology* 306:280–288.
39. Ceres P, Stray SJ, Zlotnick A (2004) *J Virol* 78:9538–9543.
40. Rossmann MG, Erickson JW (1985) in *Virus Structure and Assembly*, ed Casjens S (Jones and Bartlett, Boston), pp 29–74.
41. Johnson JM, Willits DA, Young MJ, Zlotnick A (2004) *J Mol Biol* 335:455–464.
42. Kegel WK, van der Schoot P (2004) *Biophys J* 86:3905–3913.
43. McPherson A (2005) *BioEssays* 27:447–458.
44. Zlotnick A, Aldrich R, Johnson JM, Ceres P, Young MJ (2000) *Virology* 277:450–456.
45. Smith DR, Pendry JB, Wiltshire MCK (2004) *Science* 305:788–792.
46. Riikonen S, Romero I, Garcia de Abajo FJ (2005) *Phys Rev B* 71.
47. Shvets G, Urzhumov YA (2005) *J Opt A* 7:S23–S31.
48. Maxwell-Garnett JC (1904) *Phil Trans Royal Soc* 203:385–420.
49. Prodan E, Radloff C, Halas NJ, Nordlander P (2003) *Science* 302:419–422.
50. Sun JC, Duffy KE, Ranjith-Kumar CT, Xiong J, Lamb RJ, Santos J, Masarapu H, Cunningham M, Holzenburg A, Sarisky RT, *et al.* (2006) *J Biol Chem* 281:11144–11151.
51. Hovmoller S (1992) *Ultramicroscopy* 41:121–135.
52. Ludtke SJ, Baldwin PR, Chiu W (1999) *J Struct Biol* 128:82–97.
53. Pettersen EF, Goddard TD, Huang CC, Couch GS, Greenblatt DM, Meng EC, Ferrin TE (2004) *J Comput Chem* 25:1605–1612.
54. Natarajan P, Lander GC, Shepherd CM, Reddy VS, Brooks CL, Johnson JE (2005) *Nat Rev Microbiol* 3:809–817.